



Power Electronic Systems
Laboratory

© 2015 IEEE

Proceedings of the IEEE Energy Conversion Congress & Expo (ECCE USA 2015), Montreal, Canada, September 20-24, 2015

Analysis of a Watt-Range Contactless Electromechanical Energy Harvester Facing a Moving Conductive Surface

M. Flankl,
A. Tüysüz,
J. W. Kolar

This material is published in order to provide access to research results of the Power Electronic Systems Laboratory / D-ITET / ETH Zurich. Internal or personal use of this material is permitted. However, permission to reprint/republish this material for advertising or promotional purposes or for creating new collective works for resale or redistribution must be obtained from the copyright holder. By choosing to view this document, you agree to all provisions of the copyright laws protecting it.



Eidgenössische Technische Hochschule Zürich
Swiss Federal Institute of Technology Zurich

Analysis of a Watt-Range Contactless Electromechanical Energy Harvester Facing a Moving Conductive Surface

Michael Flankl, Arda Tüysüz and Johann W. Kolar
Power Electronic Systems Laboratory
Swiss Federal Institute of Technology (ETH Zurich),
Physikstrasse 3
8092 Zurich, Switzerland

Abstract—A watt-range contactless electromechanical energy harvester based on the interaction of a rotating permanent magnet wheel with a moving conductive surface is analyzed, modeled and optimized. The extracted models are verified with two-dimensional (2-D) finite-element-method (FEM) simulations and measurement results. Finally, a $\rho\eta$ -Pareto optimization indicates a power density of the harvester wheel in the range of 2 W/cm^3 for surface speeds of 10 m/s and an air gap of 3 mm .

I. INTRODUCTION

Energy harvesting is the process of utilizing ambient energy sources for power supply purposes [1], e.g. for locally supplying devices such as sensors and actuators. In literature, temperature gradients [2], radiation [3,4], mass flow [5,6] and kinetic energy [7] are utilized for energy generation. A mechanical resonant system which extracts power from vibration is the most commonly proposed topology in case kinetic energy [8] generation and the extracted power is typically in the micro or milliwatt range [9]. For higher power systems, contactless generators are gaining importance and could also be used for regenerative braking [10] besides energy harvesting.

Shifting the extracted power levels from milliwatts to watts opens up a fascinating new area of remote, self-powered systems. Not only remote sensors and electronic systems, but also loads with higher power demand such as remote actuators could be supplied.

This paper describes a contactless electromagnetic energy harvester that can be used for watt-range energy generation, where the ambient energy source is the kinetic energy of a moving, electrically conductive body in the vicinity of the harvester. Permanent magnets mounted on a shaft that is free to rotate around its axis, are used to induce eddy currents in the moving body. The reaction force acting on the magnets makes the shaft and magnets rotate, enabling electrical power to be extracted using a stationary coil wound around the magnets. **Fig. 1** illustrates the system under consideration and

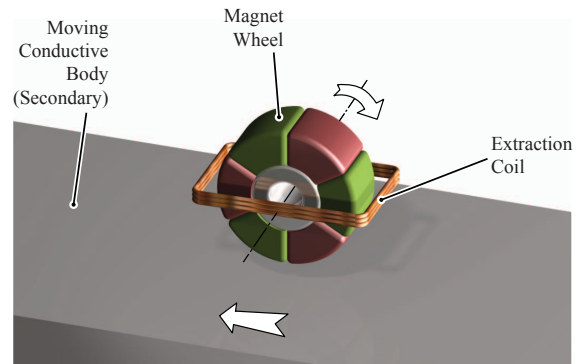


Fig. 1. Arrangement of the watt-range contactless electromechanical energy harvester. Permanent-magnet sectors magnetized radially outwards and radially inwards are arranged alternately on a shaft. The axis of rotation is aligned orthogonal to the direction of the speed of a moving body and parallel to its surface, such that a sufficient air gap is remaining. The white arrows denote the directions of rotation and translation, respectively.

is proposed in [11] for powering a low-power lighting unit, but to the best knowledge of the authors, a systematic analysis of this system has not been presented in literature so far.

Therefore, a comprehensive technical analysis of the energy harvester is carried out in this paper. Firstly, the principle of operation is described in detail in **Sec. II**. Finite-Element-Method (FEM) models are used for obtaining insight into the system's operation and for predicting the performance. Furthermore, a simplified lumped-parameter model is derived in **Sec. II-C**. The model serves as a basis for optimal control of the harvester, which ensures the maximum power extraction under all operating conditions while the limits of operation of the harvester are considered. Subsequently, a test setup is designed and constructed to evaluate the performance of the system under a wide range of operating conditions. The measurements verify the validity of the developed models. A summary of the test setup and measurement results are given in **Sec. III**. Finally, a multiobjective ρ (power density)- η (efficiency)-Pareto optimization is performed and considerations for an optimal design are summarized in **Sec. IV**.

II. PRINCIPLE OF CONTACTLESS ELECTROMECHANICAL ENERGY HARVESTER

In **Fig. 1** one can see the basic concept of the analyzed system. A wheel with radially magnetized sector magnets, the magnet wheel, is free to rotate and supported by a not depicted shaft. A stationary extraction coil surrounds the magnetic wheel and links the flux thereof. The magnet wheel itself interacts over an air gap with the moving conductive body. Key benefit of the system is that the moving body, whose kinetic energy is the primary energy source, stays untouched and the power is extracted electromagnetically over the air gap. For convenience, the moving conductive body is referred to as secondary in the following.

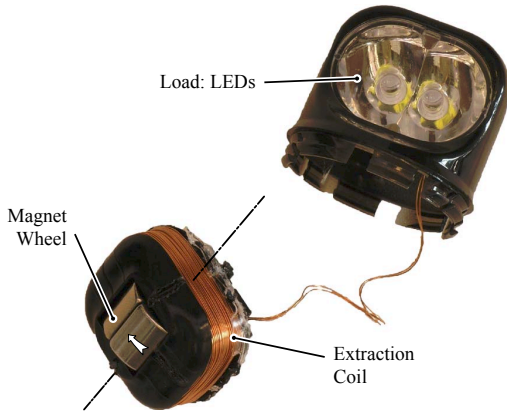


Fig. 2. Contactless harvester according to [12] with opened case. In the proposed application [11], the shown system is mounted close to an electrically conductive rotating metal ring i.e. kinetic energy is harvested. The extraction coil is directly connected to a pair of antiparallel LEDs, forming a contactless self-powered lighting unit.

The principle of operation is twofold. Firstly, kinetic power is extracted from the secondary which makes the magnet wheel spin. The interaction is based on eddy currents induced in the secondary, as will be explained in detail in **Sec. II-A**. Secondly, the mechanical power of the rotating magnet wheel is converted into electric power. The analyzed arrangement of magnet wheel and extraction coil forms an air-cored single-phase permanent-magnet synchronous generator. In other words, the permanent magnets on the magnet wheel are utilized for both, the kinetic energy extraction from the moving conductive surface (secondary) and the electromagnetic power conversion, leading to a compact design.

A. Kinetic Energy Extraction

The functional principle of the kinetic energy harvester is very similar to the concept of eddy current couplers [13]. Eddy currents are induced in the secondary due to body movement and therefore a torque is generated in combination with the magnetic field of the magnet wheel. This provides a transfer of kinetic energy from the moving body in a contactless

fashion; accordingly, the system actually forms a non-coaxial eddy current coupler comprising the magnet wheel and the secondary.

In order to excite eddy currents in the secondary, a non-zero time derivative of the magnetic flux must act on the conductive matter. For clarifying the principle of operation, one may consider a loading of the energy harvester. For higher harvester output power the difference of the surface speeds (slip) of secondary and magnet wheel will increase and after sufficient time the magnitude of induced eddy currents will settle at a higher level, i.e. a new stationary operating point will be reached.

The magnitude of the eddy currents directly determines the Lorenz force built up in the conductive matter and/or the torque acting on the magnet wheel (T_1). With the mechanical rotating frequency of the magnet wheel (ω_1), the extracted kinetic power is

$$P_{1,\text{mech}} = T_1 \omega_1. \quad (1)$$

Generally, the torque T_1 can be described as a function $T_1 = T_1(\omega_1)$ for constant speed of the secondary surface v_2 and furthermore depends on the harvester geometry, the air gap g and material parameters (according to **Fig. 3**). As confirmed with FEM simulations and measurements, T_1 can be approximated accurately as a linear function of the speed difference

$$T_1 = k_{\text{torque}} \cdot (\omega_{1,0} - \omega_1), \quad (2)$$

where $\omega_{1,0}$ is the no-load rotating speed obtained from measurements or simulations. Moreover, one can define a slip s (according to the slip definition used for induction-type machines),

$$s = \frac{\omega_1 - \omega_0}{\omega_1}, \quad (3)$$

(where $s < 0$ expresses a generative operation mode of the electric machine) with ω_1 being the magnet wheel mechanical rotational speed and ω_0 the synchronous rotational speed where no kinetic power is extracted;

$$\omega_0 = \frac{v_2}{r_1 + g}, \quad (4)$$

where v_2 is the secondary surface speed, r_1 is the radius of the magnet wheel and g is the air gap. For the no-load speed $\omega_{1,0} \leq \omega_0$ and $s \leq 0$ holds. As depicted in **Fig. 9**, a no-load slip ($\omega_1 = \omega_{1,0}$) of $s_0 \approx -0.2$ occurs for the tested system. The deviation of s_0 from zero is on one hand consequence of losses due to eddy currents induced in the secondary also for no-load operation and on the other hand caused by the definitions (3) and (4), which are not fully characterizing the speed properties of a non-constant air gap.

With 2-D FEM simulations depicted in **Fig. 3**, the kinetic energy extraction is analyzed in a time-efficient and accurate way. Since the system under consideration has a sufficient depth (l_z , orthogonal to the simulation plane) to pole pitch ($\tau = r_1 \pi / p$) ratio, the system can be analyzed in 2-D. A

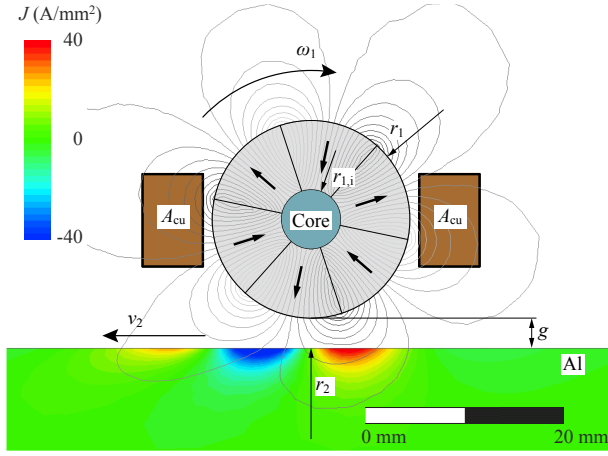


Fig. 3. Cross section of the harvester interacting with a moving aluminum secondary. As results of the 2-D FEM simulation, induced currents in aluminum and flux lines are shown. The magnet wheel rolls off the secondary while an air gap $g = 3$ mm is ensured. Arrows indicate the direction of the magnetization of the magnets; A_{cu} is the winding cross section.

fully parametric simulation model allows to investigate the influence of the slip s , the number of pole pairs p , the magnet wheel outer radius r_1 and the radius of the core $r_{1,i}$. In the simulation, the secondary with surface speed

$$v_2 = r_2 \omega_2 \quad (5)$$

is modeled as wheel with sufficient radius $r_2 (\geq 6 r_1)$. Its motion is implemented with a moving mesh, whereas the rotation of the magnet wheel ω_1 is implemented with a stationary mesh and a time dependent magnetization function. A transient simulation is conducted and only the solution after the system reaches steady-state is considered. The simulation setup allows eddy-current excitation in the secondary, whereas eddy currents in the permanent magnets and the core (the interior of the magnet wheel according to **Fig. 3**) are neglected.

Due to the nature of 2-D simulations, the FEM results are per length quantities (indicated with an apostrophe ') and can be scaled with the depth (l_z). Moreover, the simulation returns the per-length torques T'_1 (acting on the magnet wheel) and T'_2 (acting on the secondary) and therefore, the mechanically extracted power can be calculated as

$$P_{1,\text{mech}} = \underbrace{P'_{1,\text{mech}}}_{T'_1 \omega_1} l_z \quad (6)$$

and the power supplied to the secondary as

$$P_2 = \underbrace{P'_2}_{T'_2 \omega_2} l_z. \quad (7)$$

Finally, key results for the kinetic energy extraction are mechanical power density,

$$\rho_{\text{mech}} = \frac{P'_{1,\text{mech}}}{r_1^2 \pi}, \quad (8)$$

and mechanical efficiency,

$$\eta_{\text{mech}} = \frac{P'_{1,\text{mech}}}{P'_2}. \quad (9)$$

B. Electromechanical Power Conversion

As stated, the kinetic power is converted into electrical power as in a single-phase synchronous generator where the magnets on the rotating magnet wheel induce voltage in a stationary extraction coil (cf. **Fig. 1**). In the coil, a voltage is induced according to $\nabla \times \vec{E} = -\frac{\partial \vec{B}}{\partial t}$.

The root-mean-square value of the induced voltage can be expressed as

$$U_{\text{ind}} = \omega_1 p \Psi_{\text{rms}}, \quad (10)$$

where p is the number of poles and Ψ_{rms} is the flux linkage root-mean-square value of the extraction coil. Since the kinetic power extraction on average supplies the power drawn from the induced voltage, P_{ind} , the following power balance must hold for a resistive loading of the harvester

$$T_1 \omega_1 = P_{1,\text{mech}} = P_{\text{ind}} = U_{\text{ind}} I_q = \underbrace{U_{\text{cl}} I}_{P_{\text{cl}}} + R_w I^2, \quad (11)$$

where I_q is the current in phase with U_{ind} , U_{cl} the voltage across the harvester clamps (extraction coil terminals) and R_w the extraction coil winding resistance, which can be expressed as

$$R_w = \frac{N^2 \bar{l}_w}{\kappa_{\text{Cu}} A_{\text{Cu}} k_f}, \quad (12)$$

where N is the number of turns, \bar{l}_w is the average length of a winding layer, A_{Cu} the copper cross section according to **Fig. 3** and k_f the copper filling factor. The winding inductance can be expressed as

$$L_w = \frac{N^2}{R_m} \quad (13)$$

where R_m is the magnetic reluctance. The impedance $\omega_1 p L_w$ is small (the decisive magnetic reluctance R_m is high since the coil flux closes in air) compared to the winding resistance R_w and the later introduced resistance R_s for appearing frequencies at a typical energy harvesting operating point (OP). For the OP: $v_2 = 10$ m/s, $g = 3$ mm and $s = -1$, of the considered (measured) harvester, the argument of the impedance $Z_i = R_s + R_w + j\omega L_w$ is $\arg(Z_i) = 5.7^\circ$ and it seems justified to neglect L_w in the simplified equivalent circuit **Fig. 4(b)**.

Basically, the design of the electromechanical power conversion is the design of a low-power synchronous generator, where only a limited angle of the rotor circumference can be utilized. The harvester considered in this work is a compact and robust system and the coil is wound over 180° mechanical, which coincides to 3τ electrical. The coil resistance R_w could be reduced with reducing the coil pitch to 1τ due to a reduced length \bar{l}_w . Furthermore, the voltage extraction could be improved by increasing the permanent-magnet flux linkage by introducing a back-iron (not shown). Moreover, the

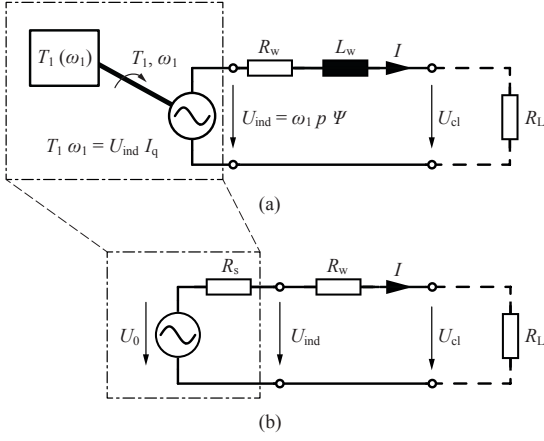


Fig. 4. (a) Detailed model showing the kinetic power extraction separated from the operation of the single-phase synchronous generator. (b) Sufficiently accurate and simplified equivalent circuit representation of the system.

system could be extended to a full three-phase synchronous generator as described in [14]. However, for a typical watt-range energy-harvesting setup ($g = 3$ mm), the kinetic power transfer is found to be the most significant limit for the overall performance; therefore, a more detailed analysis of the electromechanical power conversion is omitted in this paper.

C. Equivalent Circuit

Assuming T_1 to be a linear function of ω_1 as in (2) (verified later), negligible current orthogonal to the induced voltage U_{ind} ($I_d \approx 0$), and considering the power balance (11), the coupled electromechanical model given in Fig. 4(a) can be redrawn as in Fig. 4(b).

The equivalent circuit's inner voltage source U_0 models the no-load voltage of the system

$$U_0 = \omega_{1,0} p \Psi_{\text{rms}}. \quad (14)$$

Furthermore, the resistance R_s models the voltage drop due to slip s in the kinetic energy extraction and is derived as

$$R_s = \frac{(p \Psi_{\text{rms}})^2}{k_{\text{torque}}}, \quad (15)$$

which allows to establish a link to the torque model given in (2).

III. TEST SETUP AND MEASUREMENT RESULTS

In order to verify the FEM and equivalent circuit models, a test setup is built to take measurements with the harvester according to [12] in a wide operating range. The setup depicted in Fig. 5 allows to adjust the secondary speed and the air gap. Instead of a linear moving secondary, a secondary wheel with sufficient radius $r_2 = 100$ mm is placed. Table I summarizes the key parameters of the test setup. The harvester is loaded with a variable resistor R_L in order to take various

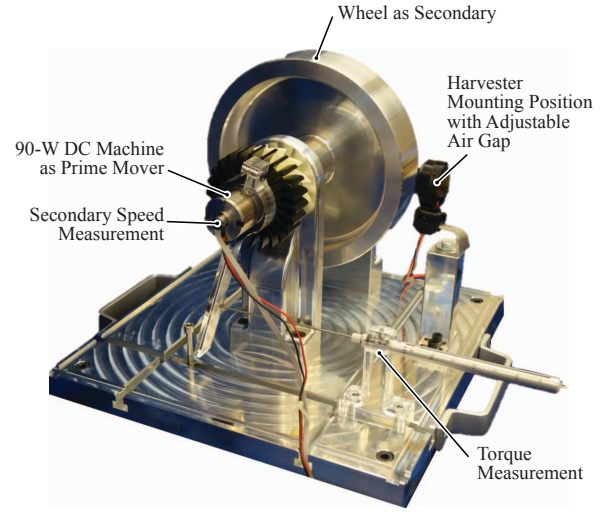


Fig. 5. Test setup for testing the harvester according to [12]. Instead of a linear moving secondary, a wheel with sufficient radius $r_2 = 100$ mm is mounted and driven by a DC machine. The harvester is then mounted on the radial surface of the secondary wheel with adjustable air gap.

measurement points in the U - I plane. Output voltage U_{cl} and current I are measured to determine the output power and a frequency measurement of the output voltage determines the rotational speed of the magnet wheel. Reaction torque on the system's prime mover (cf. Fig. 5) and rotational speed ω_2 of the secondary wheel are measured to determine the input power P_2 .

TABLE I
PARAMETERS OF THE TEST SETUP AND MEASURED RANGES.

Parameter	Variable	Value
Outer radius of magnet wheel	r_1	9 mm
Inner radius of magnet wheel	$r_{1,i}$	4 mm
Depth of magnet wheel	l_z	12 mm
Magnet wheel core material		Air
Magnet material		N52
Magnet coeiffity ^a	H_{cb}	1035 A/mm
Magnet remanence ^a	B_r	1.47 T
Radius of secondary wheel	r_2	100 mm
Depth of secondary wheel	h_1	45 mm
Secondary material		Al: EN AW-6082 (Ac-112)
Secondary conductivity ^a	κ_2	24...32 MS/m
Secondary permeability	μ_2	μ_0
Secondary surface speed	v_2	5...20 m/s
Air gap	g	3...18 mm
Number of pole pairs	p	3
Measured coil resistance	R_w	10.5 Ω
Measured coil inductance	L_w	4.3 mH

^a Datasheet value.

A. Measurements on Equivalent Circuit Modeling Approach

Firstly, electrical measurement results are presented which show that the derived modeling approach holds. Measurements given in Fig. 6 verify that the system under consideration can be represented as equivalent voltage source according to Fig. 4(b).

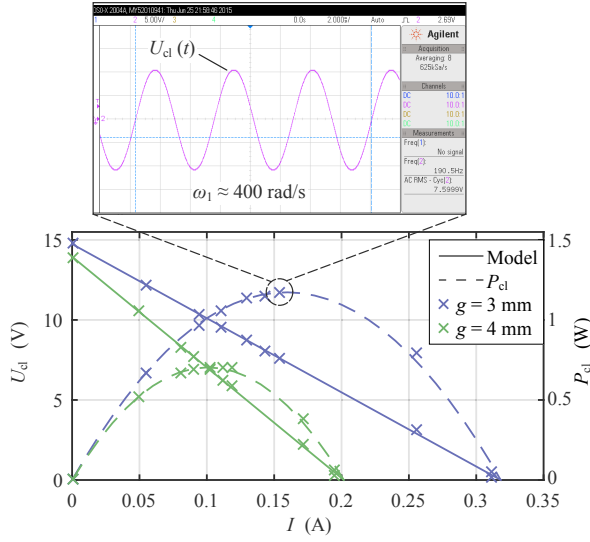


Fig. 6. Measured quantities at the harvester terminals. The bottom plot shows the output behavior of the harvester, which can be represented with an equivalent voltage source with inner resistance. In the top plot, the waveform $U_{cl}(t)$ is shown for a selected measurement point. Aluminum is used as secondary material for measurements while the surface speed was $v_2 = 10$ m/s. The air gap g was stepped according to the plot legend.

The claimed inner voltage dependency given in (10) can be confirmed with measurements taken over a secondary speed range as depicted in **Fig. 7**. In addition, the maximal induced power, calculated with measurement data as

$$P_{ind,max} = \frac{U_0^2}{4R_s}, \quad (16)$$

is shown. Of course, (and due to (11)) $P_{ind,max}$ can also be interpreted as maximal available power provided by the interaction between magnet wheel and secondary.

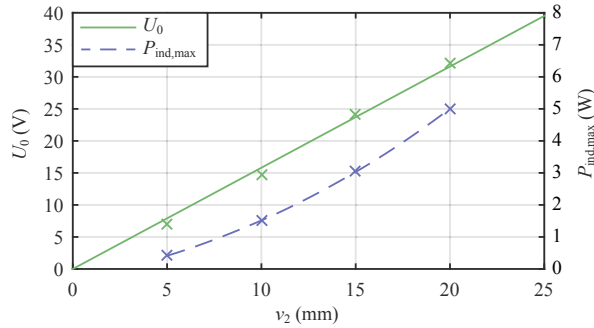


Fig. 7. Measurements over a range of secondary surface speeds v_2 and with constant air gap $g = 3$ mm. The inner voltage U_0 of the equivalent circuit is estimated and plotted. It can be seen that the modelling according to (14) holds. Moreover, the maximal induced power $P_{ind,max}$ is shown over speed.

Moreover, the resistance R_s describes the said interaction further. Its dependence on the air gap (g) is shown in **Fig. 8**. Also $P_{ind,max}$ according to (16) is given and it can be observed that the maximal induced power declines strongly

with increasing air gap g .

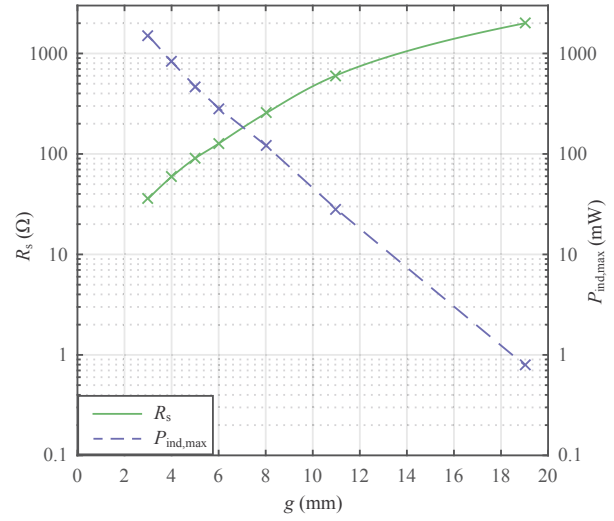


Fig. 8. For $v_2 = 10$ m/s the resistance R_s modelling the drop in induced voltage U_{ind} is estimated from measurements and shown in dependency of the air gap g . Moreover, the maximal induced power $P_{ind,max}$ is shown over air gap.

B. Verification of FEM Simulation

The principle of operation is presented in previous sections and measurement results are presented above. As described, the system is also modeled with 2-D FEM simulations and in this section the simulations are compared to measurements. Following the verification of the FEM models a multi-objective optimization is presented in the next section.

The FEM simulation gives insight in the kinetic power extraction and one can obtain the torque T_1 applied on the magnet wheel for a set of simulation parameters. However, T_1 cannot be measured directly on the test setup, but can be estimated with the power balance (11),

$$T_1 = \frac{P_{cl} + R_w \cdot I^2}{\omega_1}. \quad (17)$$

A comparison of values of T_1 from measurements, from the equivalent circuit model given in **Fig. 4(b)** and from 2-D FEM simulations is given in **Fig. 9**. The small mismatch between simulation and measurements is due to

- uncertainties in material parameters such as secondary conductivity ($\kappa_2 = 26$ MS/m assumed for the simulation) and magnet properties,
- effects at the axial ending of the magnet wheel, which are not covered in the 2-D simulation,
- friction in the bearings supporting the magnet wheel, and
- measurement inaccuracies.

Even though a small mismatch between the simulation and measurement results, it can be concluded that 2-D FEM

simulations are a fast and accurate tool for modeling and optimizing of the energy harvester topology at hand.

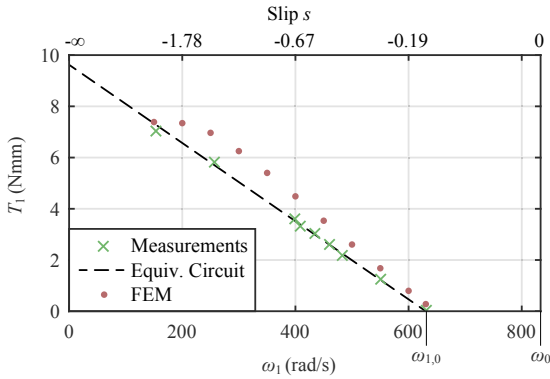


Fig. 9. Torque on magnet wheel over rotating frequency ω_1 for $v_2 = 10$ m/s and $g = 3$ mm. The torque calculated from measurement results, equivalent circuit model and 2D-FEM simulation are depicted in the figure. It can be found that the mismatch between simulation and measurements is small and it can be concluded that 2-D FEM simulations are a fast and accurate tool for modelling the kinetic power extraction.

IV. OPTIMAL DESIGN

The 2-D FEM models verified in the preceding section are used here for the $\rho\eta$ -Pareto optimization of the harvester. As mentioned earlier, only the kinetic energy extraction, which is the interaction of magnet wheel and secondary, is considered and the design of the electromechanical power conversion, comprising magnet wheel and coil interaction, is omitted. The purpose of this simulation is to explore the harvester design space comprising the magnet wheel radius r_1 , the number of pole pairs p and the radius $r_{1,i}$ of an iron core inside the magnet wheel as depicted in **Fig. 3** with regard to the performance figures power density ρ_{mech} and efficiency η_{mech} , which are finally shown in an $\rho\eta$ -plane (performance space). Moreover, for a given harvester design, the operating slip s affects the performance and is therefore also included in the optimization. The coordinates of the design space and further parameters for the conducted 2-D FEM simulations are summarized in **Table II**. All possible combinations in the space $\{r_1, r_{1,i}, p, s\}$, are simulated and evaluated (grid search).

The outcome of the simulations and measurement results of the harvester according to [12] are depicted in **Fig. 10**, where the power density and the efficiency are calculated as stated in (8) and (9) respectively. Every simulated point in the design space is evaluated and depicted as a slip-color-coded dot. It can be found that systems with similar number of pole pairs p form clouds in the performance space. Systems with higher p show better performance in efficiency η_{mech} .

For the given design space, the efficiency of the presented energy harvester topology turns out to be limited to values $< 50\%$. Accordingly, a task of further research is to obtain insight into this limitation, since it is not expected to be a

TABLE II
PARAMETER SET FOR THE PARETO ANALYSIS.

Parameter	Variable	Value
Outer radius of magnet wheel	r_1	{5, 6, 7, 8, 10, 11, 13, 15, 18, 21, 25} mm
Iron core radius	$r_{1,i}$	{0, 0.05...0.95} r_1
Secondary surface speed	v_2	10 m/s
Air gap	g	3 mm
Number of pole pairs	p	{1, 2, 3, 4}
Slip	s	{-1.25, -1, -0.75, -0.5, -0.2}
Secondary material		Aluminum
Secondary conductivity	κ_2	38 MS/m
Secondary permeability	μ_2	μ_0
Magnet material		N52
Magnet coeicity	H_{cb}	1035 A/mm
Magnet remanence	B_r	1.47 T
Magnet conductivity	κ_{mag}	0 MS/m
Magnet wheel core material		Iron
Core material conductivity	$\kappa_{1,i}$	0
Core material permeability	$\mu_{1,i}$	4000 μ_0

strict physical limit. It is also observed that the Pareto front is rather flat with respect to the ρ - η trade-off.

For one specific harvester geometry, defined by r_1 , $r_{1,i}$ and p , a trajectory in the $\rho\eta$ -plane can be observed when varying the slip s . Those trajectories are depicted for three selected systems (Sys. A - C) in **Fig. 10** and the systems' key parameters are summarized in **Table III**.

- System A was selected as optimized for minimal losses ($\eta_{\text{mech}} \approx 48\%$) with reasonable power density, where the most suitable operating point is with $s = -0.75$.
- System B is a high power density system with ($\rho_{\text{mech}} \approx 2.3$ W/cm³) and $p = 2$.
- Unfortunately, systems A and B are not suitable for low power applications, although they show best results in the ρ - η -plane because their per-length power $P'_{1,\text{mech}}$ is high, leading to systems with too small axial length ($l_a < 1$ mm) for power targets of $P_{1,\text{mech}} < 10$ W. Therefore, system C is presented as a compact system for low power targets. Surprisingly, for system C both the power density and the efficiency decrease with decreasing slip.

TABLE III
KEY PARAMETERS OF SELECTED SYSTEMS A-C

Parameter	Sys. A	Sys. B	Sys. C
p	3	2	1
r_1	25 mm	18 mm	8 mm
$r_{1,i}$	15 mm	9 mm	2.4 mm
s_{opt}	-0.75	-1	-1.25
ρ_{mech}	1.35 W/cm ³	2.32 W/cm ³	2.26 W/cm ³
η_{mech}	47.9%	39.1%	25.4%
$P'_{1,\text{mech}}$	2.64 W/mm	2.36 W/mm	0.45 W/mm

V. CONCLUSION

A watt-range contactless electromechanical energy harvester is presented and analyzed theoretically and experimentally.

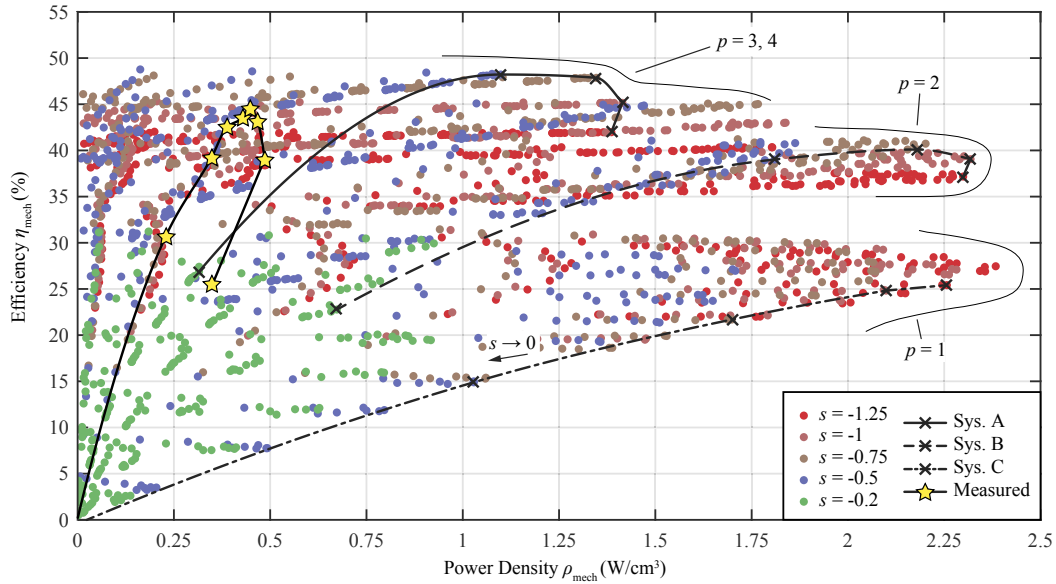


Fig. 10. Pareto analysis of the kinetic power extraction in a mechanical power density ρ_{mech} - mechanical efficiency η_{mech} plain. 2-D FEM simulations are conducted according to the parameter set **Table II**. Moreover, measurement results of the harvester according to [12] are also shown.

The peak electric output power at the terminals of the system with volume $V \approx 14 \text{ cm}^3$ is measured as $P_{\text{cl}} > 4 \text{ W}$ for an air gap of $g = 3 \text{ mm}$ and a secondary surface speed of $v_2 = 20 \text{ m/s}$. A detailed analysis shows that the principle of operation can be split into kinetic power extraction based on eddy current coupling and electromechanical power conversion with a single-phase synchronous generator. The kinetic power extraction is analyzed with 2-D FEM simulations and after a verification with measurements, a multiobjective $\rho\eta$ -analysis and Pareto optimization is conducted therefore. The optimization indicates a power density of the harvester wheel in the range of 2 W/cm^3 for surface speeds of 10 m/s and air gap of 3 mm .

In summary, the given analysis shows at the example of optimal designs (Sys. A-C) that the concept allows to harvest energy from a moving conductive body in a contactless fashion over a comparable large air gap ($g = 3 \text{ mm}$) and is suitable for different industry and consumer applications.

REFERENCES

- [1] O. Kanoun, J. Wallaschek et al., *Energy Harvesting*. Expert Verlag, 2008.
- [2] H. Lhermet, C. Condemine, M. Plissonnier, R. Salot, P. Audebert, and M. Rosset, "Efficient power management circuit: From thermal energy harvesting to above-ic microbattery energy storage," *IEEE Journal of Solid-State Circuits*, vol. 43, no. 1, pp. 246–255, Jan 2008.
- [3] D. Brunelli, C. Moser, L. Thiele, and L. Benini, "Design of a solar-harvesting circuit for batteryless embedded systems," *IEEE Transactions on Circuits and Systems I: Regular Papers*, vol. 56, no. 11, pp. 2519–2528, Nov 2009.
- [4] M. Midrio, S. Boscolo, A. Locatelli, D. Modotto, C. De Angelis, and A.-D. Capobianco, "Flared monopole antennas for $10 \mu\text{m}$ energy harvesting," in *2010 European Microwave Conference (EuMC)*, Sept 2010, pp. 1496–1499.
- [5] E. Sardini and M. Serpelloni, "Self-powered wireless sensor for air temperature and velocity measurements with energy harvesting capability," *IEEE Transactions on Instrumentation and Measurement*, vol. 60, no. 5, pp. 1838–1844, May 2011.
- [6] J. Azevedo and F. Santos, "Energy harvesting from wind and water for autonomous wireless sensor nodes," *Circuits, Devices Systems, IET*, vol. 6, no. 6, pp. 413–420, Nov 2012.
- [7] G. Szarka, B. Stark, and S. Burrow, "Review of power conditioning for kinetic energy harvesting systems," *IEEE Transactions on Power Electronics*, vol. 27, no. 2, pp. 803–815, Feb 2012.
- [8] D. Zhu, S. Beeby, "Kinetic Energy Harvesting," in *Energy Harvesting Systems: Principles, Modeling and Applications*, ch. 1, T. J. Kazmier-ski, S. Beeby, Ed. Springer, 2011.
- [9] S. Beeby, T. O'Donnell, "Electromagnetic Energy Harvesting," in *Energy Harvesting Technologies*, ch. 5, S. Priya, D. J. Inman, Ed. Springer, 2009.
- [10] T. Krupenkin and J. A. Taylor, "Reverse electrowetting as a new approach to high-power energy harvesting," *Nature Communications*, vol. 2, no. 448, Aug 2011.
- [11] D. Strothmann, "Device for contactless current generation, in particular bicycle dynamo, vehicle lighting system and bicycle," DE Patent WO 2013/004 320 A1, 01 10, 2013.
- [12] Magnic Innovations GmbH & Co KG. checked: 07.07.2015. [Online]. Available: <http://www.magniclight.com>
- [13] E. Davies, "An experimental and theoretical study of eddy-current couplings and brakes," *IEEE Transactions on Power Apparatus and Systems*, vol. 82, no. 67, pp. 401–419, Aug 1963.
- [14] Shun-Fu Technology Corp., "Induktionsgenerator," Gebrauchsmuster DE 202 014 100 380 U1, 04 24, 2014.